Available online at www.CivileJournal.org

Civil Engineering Journal

(E-ISSN: 2476-3055; ISSN: 2676-6957)

Vol. 12, No. 05, May, 2026

CFD-Based PSO Optimization of Bamboo Roof Trusses Under Wind Loading

Nurwin Adam G. Muhammad [1, 2], Jerson N. Orejudos [3], Mary Joanne C. Aniñon [4], Lessandro Estelito O. Garciano [4*]

[1] *Department of Civil Engineering, Western Mindanao State University, Zamboanga City 7000, Philippines.*

[2] *Graduate School, Mindanao State University–Iligan Institute of Technology, Philippines, Iligan City 9200, Philippines.*

[3] *Department of Civil Engineering, Mindanao State University–Iligan Institute of Technology, Iligan City 9200, Philippines.*

[4] *Department of Civil Engineering, Gokongwei College of Engineering, De La Salle University, Manila 1004, Philippines.*

Received 30 January 2026; Revised 23 April 2026; Accepted 26 April 2026; Published 01 May 2026

Abstract

Bamboo roof trusses are promising for low-carbon housing, but their performance under strong wind is highly influenced by roof geometry. This study developed a coupled computational fluid dynamics (CFD) and particle swarm optimization (PSO) framework to optimize a bamboo Howe roof truss under extreme wind loading. The objective was to reduce the maximum member utilization by finding a roof-truss geometry that responds efficiently to geometry dependent wind effects. For each candidate geometry, ANSYS SpaceClaim and ANSYS Fluent were used to update the roof profile and compute the wind-induced force resultants acting on the roof surfaces. These force resultants, together with roof and ceiling dead loads, were then applied to a MATLAB two-dimensional frame model to calculate member forces, deflections, and utilization ratios. The PSO run converged after 660 objective-function evaluations over 22 iterations using 30 particles per iteration. The optimized truss had a ridge height of h_r = 2.079 m, r_1 = 0.324, and r_2 = 0.487, giving a maximum member utilization of 0.116, small deflection, and a truss volume of approximately 0.05 m³. Compared with the best solution in the first iteration, the optimized design reduced maximum utilization by 37%. The main contribution of this study is the integration of CFD derived wind loading with PSO-based bamboo truss optimization, allowing both wind demand and structural response to be updated during the search process.

Keywords: Bamboo Structures; Roof Trusses; Structural Optimization; Particle Swarm Optimization; Wind Loading.

1. Introduction

The global demand for housing continues to exceed supply, particularly in developing countries and tropical regions where rapid urbanization, population growth, and exposure to natural hazards converge [1]. At the same time, the construction sector remains a major contributor to global carbon emissions, largely due to the widespread reliance on carbon-intensive materials such as cement and steel [2]. These realities have intensified efforts to identify alternative structural materials that are renewable, locally available, and capable of meeting modern performance requirements for safety and resilience [3].

Bamboo has emerged as a viable candidate in this context. It is a fast-growing, renewable resource that is widely available in tropical countries, which offers significant environmental advantages over conventional construction

* Corresponding author: lessandro.garciano@dlsu.edu.ph

https://doi.org/10.28991/CEJ-2026-012-05-023

materials [4–9]. When properly treated, bamboo exhibits favorable mechanical properties and a high strength-to-weight ratio, making it suitable for load-bearing applications [10–14]. In housing construction, bamboo has been used for walls, floors, and roof framing systems, including roof trusses that play a critical role in transferring loads to supporting elements [15].

In the Philippines, the need for resilient housing solutions is particularly pressing. According to the Philippine Atmospheric, Geophysical and Astronomical Services Administration (PAGASA), an average of about 20 tropical cyclones enter the Philippine Area of Responsibility each year, with about 8 making landfall [16]. Several of which reach typhoon or super-typhoon intensity [16]. Extreme wind speeds generated during these events impose severe demands on low-rise housing, where roof systems are consistently identified as the most vulnerable components. Wind-induced uplift forces can lead to roof detachment, progressive structural damage, and the generation of wind-borne debris, posing serious risks to life safety and post-event habitability. Consequently, improving the wind resistance of roof systems, particularly roof trusses, is essential for enhancing the resilience of housing in typhoon-prone regions.

Roof performance under wind loading is strongly influenced by geometry. Variations in roof slope, pitch, and overall configuration significantly affect air flow patterns, pressure distribution, and uplift forces acting on roof surfaces [17]. For bamboo roof trusses, which are lightweight and geometry-sensitive, this interaction between aerodynamic demand and structural response becomes even more critical. Designing bamboo trusses that can withstand extreme winds therefore requires a systematic approach that considers both wind flow behavior and structural efficiency.

1.1. Computational Fluid Dynamics Simulations for Structures Under Wind Loading

Computational fluid dynamics (CFD) is a discipline within fluid mechanics that employs numerical methods and modern computing capabilities to simulate fluid flow behavior. The origins of CFD can be traced to early theoretical developments in the 1920s, when numerical approaches were first explored for forecasting meteorology. One of the earliest and most enduring applications of CFD has been in weather forecasting, demonstrating its effectiveness in simulating wind-related phenomena relevant to the built environment [18].

With advances in computational power and numerical techniques, CFD has gradually expanded beyond meteorology into engineering applications, including wind engineering and building aerodynamics. Enhanced CFD modeling strategies have enabled more detailed evaluation of wind pressures acting on building envelopes and roof systems [17, 19–22]. As a result, CFD has become an effective tool for investigating wind-induced demands on buildings or structures subjected to strong wind events such as typhoons and super typhoons.

Several studies have demonstrated the application of CFD in assessing wind effects on roofs and overall building performance. Enteria [20] investigated various roofing designs of detached structures in the Philippines using CFD to evaluate their response under strong wind conditions. Singh & Roy [17] examined the influence of roof slope and wind direction on wind pressure distribution for a low-rise building with a pyramidal roof configuration using CFD simulations. Mata et al. [21] employed a coupled genetic algorithm (GA) and CFD framework to optimize building orientation and roof angle for a typhoon-resilient single-family house, with the objective of minimizing aerodynamic drag under a constant wind speed. More recently, Zhang et al. [22] conducted a CFD-based parametric study to optimize a Venturi-shape roof configuration in high-rise buildings for wind energy harvesting applications. Collectively, these studies demonstrate the growing use of CFD not only for wind load assessment but also for the optimization of building geometries subjected to wind loading.

Despite the proven effectiveness of CFD for evaluating and optimizing wind-exposed building components, its application to bamboo-based structural systems remains limited. In particular, the integration of CFD into design and optimization methodologies for improving wind resistance of bamboo roof trusses has not been extensively explored. This gap highlights the opportunity to extend CFD-based wind analysis frameworks to bamboo structural systems, especially in regions where bamboo is increasingly promoted as a sustainable construction material.

1.2. Particle Swarm Optimizations for Structures Under Wind Loading

Structural optimization provides a systematic and rational framework for improving structural performance by exploring a range of feasible design alternatives under defined objectives and constraints [23–27]. In structural engineering applications, optimization objectives commonly include reducing material demand, improving load-carrying efficiency, enhancing stiffness, and controlling serviceability responses such as deflection [23–27]. These objectives are particularly relevant for lightweight structural systems, where geometry strongly influences structural response [27].

Several studies have successfully applied optimization techniques to conventional structural systems. In the Philippine context, Pararuan et al. [28] employed genetic algorithm (GA) within a MATLAB-based framework to optimize reinforce concrete frame structures while ensuring compliance with the National Structural Code of the Philippines (NSCP) [29]. Although their study focused on reinforced concrete frames and cost-oriented objectives, it

demonstrated how optimization algorithms can be effectively coupled with structural analysis to address complex, multi-parameter design problems.

Recent advances in computational optimization frameworks have further enabled efficient evaluation of complex objectives and constraints. Lee et al. [30] introduced differentiable structural analysis using automatic differentiation to accelerate optimization workflows, showing how modern computational methods can improve both speed and flexibility of structural optimization. Complementary efforts have also produced compact implementations of optimization methods within MATLAB environments. Zhuang et al. [31] presented a lightweight MATLAB-based topology optimization approach, illustrating that practical and accessible implementations can support optimization studies without requiring excessive computational overhead.

Belz & Kromoser [32] highlighted that optimization-based approaches can significantly improve structural efficiency and material utilization, however, practical application often remains limited due to modeling complexity and accessibility constraints, particularly for materials and systems that require specialized modeling considerations. These challenges are directly relevant to bamboo structures, which exhibit variability and anisotropy behavior and therefore require practical computational workflows to enable optimization-based design.

Metaheuristic methods are well-suited for problems involving nonlinear behavior, discrete variables, and computationally expensive analysis [24]. Among these methods, particle swarm optimization (PSO) has gained considerable attention in structural optimization studies [33, 34]. PSO is a population-based algorithm inspired by collective social behavior such as the flocking of birds or schooling of fish, in which candidate solutions explore the design space by sharing information related to individual and collective performance [33, 34]. PSO has been successfully applied to numerous structural optimization problems, including truss design optimization involving size, shape, and topology variables across various structural cases [35–38]. However, despite its demonstrated effectiveness in conventional structural systems, the application of PSO to bio-based structural systems, particularly bamboo structures, remains limited.

1.3. Potential of Coupling CFD and PSO for Roof Truss Design Under Wind Loading

Previous studies have demonstrated the effectiveness of computational fluid dynamics (CFD) in evaluating wind-induced pressures on roof systems [17, 19–22, 39]. Other studies have also shown the capability of metaheuristic optimization techniques to improve structural performance, material efficiency, and serviceability response in different structural systems [21, 23, 28, 30, 31, 36, 38]. These works show that CFD and optimization can be powerful tools in structural design, particularly when wind demand or structural response is strongly affected by geometry. Studies on conventional materials, such as steel and reinforced concrete, have shown that coupling advanced analysis tools with optimization algorithms can lead to significant improvements in structural performance and material utilization [21].

In parallel, a growing body of literature has established bamboo as a viable material for load-bearing structural applications, including roof systems [8, 40–42]. These studies have highlighted key factors influencing bamboo structural performance, such as member variability, connection behavior, and geometric configuration [8, 40–42]. Most existing studies on bamboo structures have focused on experimental characterization [43–45] or numerical evaluation of structural response under prescribed loading conditions [46–48]. While these studies provide critical insights into bamboo material behavior and system-level performance, they generally do not extend to optimization-based design frameworks.

Although CFD-based optimization has been applied to conventional building forms and materials [21], its application to bamboo roof-truss systems remains limited. This gap is important because bamboo roof trusses are lightweight and geometry-sensitive, and their performance under strong wind depends not only on member capacity but also on how roof shape affects pressure and suction. Therefore, an optimization framework for bamboo roof trusses should account for both geometry-dependent aerodynamic demand and structural response.

To address this gap, this present study proposes a coupled CFD-PSO framework for optimizing a bamboo Howe roof truss subjected to extreme wind loading representative of Philippine typhoon conditions. In the proposed workflow, each candidate roof geometry is evaluated using ANSYS Fluent to obtain geometry-dependent wind force resultants. These wind force resultants are then transferred to a MATLAB two-dimensional frame model to compute member forces, deflections, and utilization ratios. PSO is implemented in MATLAB, which is used to search for the truss geometry that minimize peak member utilization while satisfying strength and serviceability constraints. The main contribution of this study is the integration of CFD-derived wind loading with PSO-based bamboo roof-truss optimization, allowing both wind demand and structural response to be updated for each candidate geometry.

2. Materials and Methods

This study develops a coupled computational workflow that links computational fluid dynamics (CFD) wind simulation, structural analysis, and particle swarm optimization (PSO) to improve the wind-resistant performance of a

bamboo Howe roof truss. The roof-truss geometry is parameterized by height of ridge and two dimensionless ratios that define the horizontal locations of the internal vertical members on one half of the span. For each candidate geometry, ANSYS Fluent is used to obtain wind-induced roof force resultants, and a MATLAB-based two-dimensional frame finite element model evaluates member forces, deformations, and utilization. MATLAB then executes PSO to identify the geometry that minimizes the peak member utilization while satisfying structural constraints.

Wind loading on pitched roofs is strongly influenced by roof slope and flow phenomena such as separation and suction. For this reason, a CFD-based evaluation was adopted so that aerodynamic demand is updated consistently with each candidate roof geometry rather than prescribed using a fixed pressure pattern. As shown in Figure 1, the methodology operates as a closed-loop workflow. PSO generates a set of candidate designs, and for each candidate the roof profile is updated in ANSYS SpaceClaim and analyzed in ANSYS Workbench/Fluent to obtain the wind-induced force resultants acting on the left and right roof halves. These wind resultants are then transferred to the MATLAB structural model of the Howe truss together with roof and ceiling dead loads. The structural analysis returns member forces and deformations, from which utilization ratios are computed and the objective function value is evaluated. The objective value is fed back to PSO to guide the next set of candidate designs. This cycle repeats until the stall-based convergence criterion is satisfied, after which the best-performing design is reported.

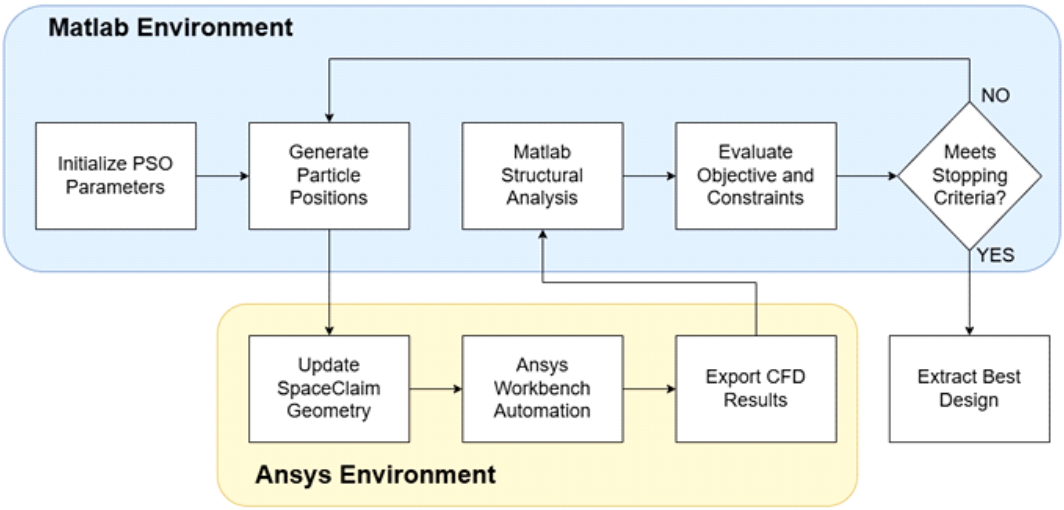

Figure 1. Methodology flowchart

The theoretical approach of this study is based on the coupled relationship between aerodynamic demand, structural response, and optimization search. Wind pressure on a pitched roof is affected by roof geometry because changes in roof slope influence flow separation, pressure distribution, and suction on the roof surfaces [17, 19–22, 39]. Therefore, the wind load was not treated as a fixed pressure pattern. Instead, CFD was used to obtain geometry-dependent wind force resultants for each candidate roof profile. These wind force resultants were then transferred to a two-dimensional frame model, where the structural response was computed using the direct stiffness method. In general form, the structural equilibrium Equation is presented as Equation 1.

$$KU = F \tag{1}$$

where, K is the global stiffness matrix, U is the global nodal displacement vector, and F is the global load vector. After solving for the nodal displacements, member forces were recovered and used to compute the utilization ratios of the truss members. The optimization problem was formulated to minimize the maximum member utilization, expressed in general form in Equation 2.

$$\min_{x} f(x) = \max_{i=1,\ldots,n_m} (UR_i) \tag{2}$$

where, x is the design-variable vector, UR_i is the utilization ratio of member i, and nm is the total number of truss members. In this framework, CFD provides the geometry-dependent aerodynamic demand, the stiffness-based structural model provides the member response, and PSO provides the search mechanism for improving the truss geometry. The detailed geometry definition, CFD setup, structural formulation, and PSO implementation are presented in the following subsections.

The two-dimensional idealization was adopted as a practical simplification for the initial development of the coupled CFD-PSO workflow. The CFD model represents the transverse section of a low-rise roof, while the structural model

represents a typical bamboo Howe roof truss in its primary load-resisting plane. This approach allowed repeated CFD and structural evaluations to be performed within a manageable computational cost during optimization. The truss was treated as an interior representative frame subjected to tributary roof loading. However, this simplification does not explicitly capture three-dimensional effects such as wind-direction variation, end-zone effects, longitudinal pressure variation, out-of-plane bracing, and connection behavior. Therefore, the results should be interpreted within the assumptions of the two-dimensional aerodynamic and structural models. Future work should extend the framework to three-dimensional CFD and structural modeling to evaluate these effects more completely.

2.1. Structural Model and Parametric Definition of Bamboo Howe Roof Truss

The bamboo Howe roof truss is represented using a two-dimensional node-member model with geometry symmetric about the midspan, as shown in Figure 2. The support-to-support span is denoted by L, and the ridge height is denoted by h_r. The geometry is parameterized by the ridge height and by the panel lengths L_1, L_2, and L_3 defined on the left half-span $(0.5L)$, which locate the interior panel points along the bottom chord; the right half is generated by mirroring about midspan.

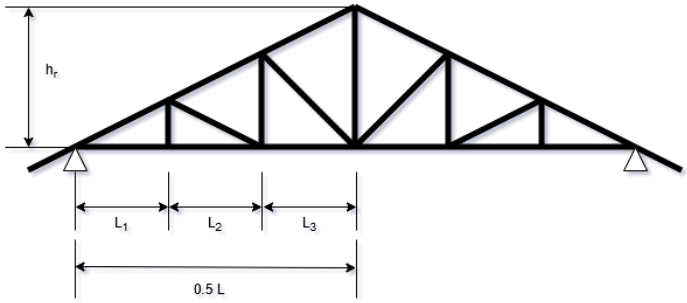

Figure 2. Bamboo Howe truss

The bottom chord was discretized into seven nodes, while the top chord consisted of five nodes. The elevations of the top chord nodes were generated by linear interpolation along the roof slope so that the roof height increases linearly from the support to the ridge on each half of the span. With this parameterization, the overall roof profile is governed by the ridge rise above the wall top, h_r, while the internal panel layout is governed by the segment lengths L_1, L_2, and L_3 defined in Equations 3 to 5.

$$L_1 = r_1(0.5L) \tag{3}$$

$$L_2 = r_2(0.5L) \tag{4}$$

$$L_3 = 0.5L - L_1 - L_2 \tag{5}$$

The house envelope shown in Figure 3 was modelled in ANSYS Fluent. The roof overhang length on each side is denoted by L_o. The wall-to-wall width is denoted by L, which is also taken as the support-to-support span of the truss. The wall height measured from the ground line to the wall to truss connection is denoted by h_w. The total height of the house to the ridge is denoted by H and is expressed in Equation 6.

$$H = h_w + h_r \tag{6}$$

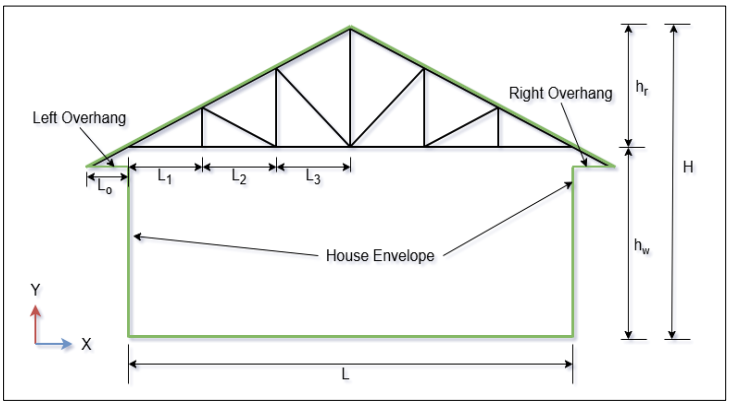

Figure 3. Definition of house envelopes and roof truss geometric parameters

2.2. Computational Fluid Dynamics (CFD) Modeling of Wind Loads in ANSYS Fluent

The CFD modeling was performed in the ANSYS Workbench environment. ANSYS SpaceClaim was used to generate the two-dimensional geometry of the house cross-section together with a surrounding wind-tunnel computational domain, while ANSYS Fluent was used to solve the external wind flow and produce the wind load resultants needed for the MATLAB structural analysis. To automate the CFD stage, two scripts were used: *main_triangle_roof_TEMPLATE.py* for geometry generation in SpaceClaim and *trialscript1.wbjn* for running the Workbench Fluent update sequence and exporting results. For every design candidate evaluated by MATLAB, a new *main_triangle_roof_TEMPLATE.py* file is written by inserting the current ridge height, h_r value into the script. In contrast, *trialscript1.wbjn* is not rewritten; MATLAB simply executes the same journal file for all candidates to run the CFD analysis and export outputs.

The *script main_triangle_roof_TEMPLATE.py* defined the fixed geometry of the house and the parameterized roof profile. The wall-to-wall width L is set to 6.0 m, the wall height h_w is set to 2.5 m, and the roof overhang L_o is set to 0.6 m on each side. After initializing a SpaceClaim document and starting a constraint sketch on the XY plane, the script sketches the house envelope and then constructs the wind-tunnel boundary that encloses the house geometry. Using height H, the upstream length is set to $5H$, the downstream length is set to $10H$, and the top clearance is set to $5H$. The horizontal extent of the roof is defined from the left overhang tip to the right overhang tip, and the wind-tunnel domain is extended upstream and downstream from these limits. The roof geometry is modelled as a symmetric triangular profile with overhang. After completing the sketch, the script switches to solid interaction mode to finalize the geometry for downstream CFD use, saves the updated model as *FFF.scdoc*, and exits SpaceClaim.

2.2.1. Boundary Identification and Wind Loading Specification

In ANSYS Workbench, boundary conditions in Fluent must be assigned to specific geometric entities such as edges in a two-dimensional model or faces in a three-dimensional model. *Named Selections* are user defined labels that tag these entities with fixed names so they can be referenced consistently during meshing, solver setup, and results extraction.

To ensure consistent boundary condition assignment in Fluent, *main_triangle_roof_TEMPLATE.py* also creates *Named Selections* that label the relevant boundaries and regions as shown in Figure 4. These include the fluid region ("Air") and edge selections for the inlet and outlet boundaries of the wind tunnel ("Inlet" and "Outlet"), the grouped top and ground boundaries ("Top_Bottom_Boundaries"), the left and right walls ("left_wall" and "right_wall"), and the roof and overhang segments on both sides ("L_roof", "R_roof", "L_overhang", and "R_overhang"). These names are preserved in the saved *FFF.scdoc* file and are subsequently available in the Fluent setup, allowing the same CFD boundary condition definitions to be applied consistently even as the roof geometry changes between design candidates. The inlet wind speed was a constant 94 meters per second. This value was obtained from National Structural Code of the Philippines (NSCP) [29]. The wind loading was unidirectional and aligned with the global x-axis.

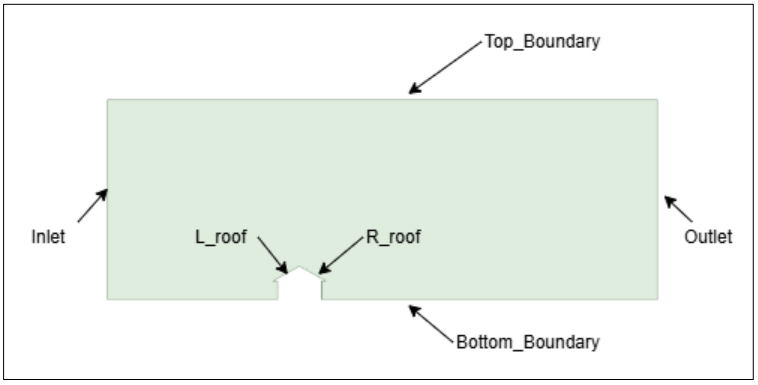

Figure 4. *Named Selections* used in ANSYS Fluent

A single wind speed was adopted to represent the extreme design wind condition considered in this study. This decision was also made to keep the CFD-coupled optimization computationally manageable, since each candidate geometry required geometry regeneration, CFD solution, extraction of roof force resultants, and structural analysis. Using one wind speed allowed direct comparison among candidate geometries under the same severe wind condition. However, this assumption limits the generalizability of the optimized geometry to other wind speeds and wind scenarios. Future work should extend the proposed framework to multiple wind speeds and wind directions to evaluate the robustness of the optimized truss configuration under a broader range of wind demands.

2.2.2. ANSYS Workbench and Fluent Execution and Export of Results

The ANSYS Workbench components used for the CFD analysis are shown in Figure 5. The CFD execution is controlled by the Workbench journal *trialscript1.wbjn*. This script opens the Workbench project file (*Main_triangle_new.wbpj*), updates the *Geometry* component by pointing it to the most recently generated SpaceClaim file (*FFF.scdoc*). The journal then updates the CFD workflow sequentially by updating the components for *Mesh*, *Setup*, *Solution*, and *Results* components with dependencies enabled, ensuring that the mesh and solution are regenerated whenever the geometry changes. The *Named Selections* created in SpaceClaim as discussed in the previous subsection were carried into Workbench and used as fixed references for boundary condition assignment in Fluent. This made it possible to apply the same inlet, outlet, wall, roof, and overhang conditions consistently for every geometry update without manual boundary selection. After the update sequence completes, the journal exports the design-point results to a CSV file (*results1.csv*) using the Workbench parameter export function. This CSV file serves as the interface back to MATLAB, where the CFD-derived outputs are read and converted into wind force resultants for structural analysis and optimization.

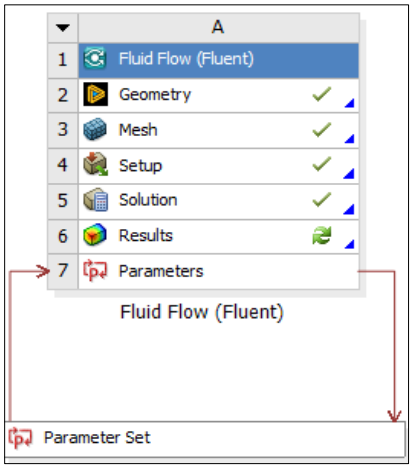

Figure 5. Ansys Workbench components for CFD Analysis

2.2.3. ANSYS Workbench and Fluent Execution and Export of Results

Several verification checks were performed to ensure consistency of the coupled CFD–structural workflow. First, the Named Selections created in ANSYS SpaceClaim were checked to confirm that the inlet, outlet, wall, roof, overhang, and fluid-domain boundaries were consistently transferred to ANSYS Workbench and Fluent for each candidate geometry. This step was important because the roof geometry changed during the optimization process, while the boundary-condition assignment had to remain consistent across all CFD evaluations.

Second, the CFD output file exported from ANSYS Workbench was checked to confirm that the wind force resultants on the left and right roof surfaces were successfully extracted and read by MATLAB. These force resultants were then converted into equivalent line loads and applied to the corresponding roof members in the structural model. Third, the MATLAB structural model was checked by confirming that support reactions, applied loads, and member-force recovery were consistent with the assembled global equilibrium system. Finally, the optimized design was checked against the imposed geometric feasibility constraints and member utilization criterion.

The present study did not include direct wind-tunnel calibration or experimental validation of the CFD model for the specific bamboo roof configuration. Therefore, the numerical results should be interpreted within the assumptions of the adopted two-dimensional CFD model, boundary conditions, and structural idealization. Future work should validate the CFD predictions against wind-tunnel tests or benchmark data for comparable low-rise roof geometries.

2.3. Structural Analysis of Bamboo Howe Roof Truss in MATLAB

2.3.1. Material Properties

Structural analysis was performed in MATLAB using a linear elastic two-dimensional frame element formulation. Each node had three degrees of freedom consisting of horizontal displacement, vertical displacement, and rotation, and the global stiffness matrix is assembled by summing the transformed element stiffness matrices of all members. Values for material properties and mechanical properties were obtained from the Philippine Guidelines on Bamboo Design and Construction 2025 [49].

Table 1 summarized the physical and mechanical properties used in the structural model. The wall thickness t and outer diameter D defined the hollow circular culm section used for all members. The modulus of elasticity E and the allowable stresses for compression, tension, bending, and shear are used to compute stiffness, member capacities, and utilization ratios.

Table 1. Material Physical and Mechanical Properties

Symbol	Property	Value	Unit
t	Wall thickness	10	mm
D	Outer diameter	80	mm
E	Modulus of elasticity	13	GPa
$F_{c-allow}$	Allowable Compressive strength	19.17	MPa
$F_{t-allow}$	Allowable Tensile strength	24.86	MPa
$F_{v-allow}$	Allowable Shear Strength	13	GPa
$F_{b-allow}$	Allowable Bending Strength	21.4	MPa

Bamboo is a naturally anisotropic and variable material; however, a linear elastic material model was adopted in this study to provide a consistent design-level comparison among candidate truss geometries. The material properties and allowable stresses were taken from the Philippine Guidelines on Bamboo Design and Construction 2025 [49], and the optimization focused on member utilization under the adopted allowable-stress framework. This assumption is appropriate for comparing relative performance among candidate geometries, but it does not explicitly capture nonlinear material behavior, strength variability, local crushing, splitting, or connection flexibility. These effects may influence the actual stiffness, member capacity, failure mode, and final optimum geometry. Therefore, the optimized configuration should be interpreted within the assumptions of the linear elastic structural model. Future work should incorporate probabilistic bamboo properties, nonlinear material behavior, and connection flexibility to evaluate the robustness of the optimized truss configuration.

2.3.2. Structural Analysis

For each element, the member length and direction cosines were computed from the nodal coordinates as given in Equations 7 and 8, which provided the cosine and sine terms used to define member orientation in the global coordinate system. respectively. The local element stiffness matrix $k_e^{(l)}$ in Equation 9 was then formed to include axial and bending contributions through the parameters, namely, modulus of elasticity, E, cross-sectional area, A, moment of inertia, I, and member length, L_m. This local stiffness matrix was transformed into the global coordinate system using the transformation relation in Equation 10, where the transformation matrix T is defined in Equation 11 and the rotation matrix R is defined in Equation 12. After transformation, the global stiffness matrix KU_e was assembled by adding the global element stiffness matrices of all members into the appropriate locations based on connectivity. The unknown global nodal displacement vector U_e was obtained by solving the global equilibrium Equations in Equation 13 after applying the support boundary conditions and assembling the global load vector F.

After obtaining the global nodal displacement vector U_e, the internal actions of each member were recovered from the element end displacements. For a member connecting nodes i and j, the element displacement vector was obtained using Equations 14. This vector was transformed from global coordinates to local member coordinates using Equation 15. The member end force vector in local coordinates was then obtained from Equation 16 by multiplying the local stiffness matrix by the local displacement vector. The axial force N, shear force V, and bending moment M were obtained using Equations 17.

$$c = \frac{x_j - x_i}{L_m} \tag{7}$$

$$s = \frac{y_j - y_i}{L_m} \tag{8}$$

$$k_e^{(l)} = \begin{bmatrix} \frac{EA}{L_m} & 0 & 0 & -\frac{EA}{L_m} & 0 & 0 \\ 0 & \frac{12EI}{{L_m}^3} & \frac{6EI}{{L_m}^2} & 0 & -\frac{12EI}{{L_m}^3} & \frac{6EI}{{L_m}^2} \\ 0 & \frac{6EI}{{L_m}^2} & \frac{4EI}{L_m} & 0 & -\frac{6EI}{{L_m}^2} & \frac{2EI}{L_m} \\ -\frac{EA}{L_m} & 0 & 0 & \frac{EA}{L_m} & 0 & 0 \\ 0 & -\frac{12EI}{{L_m}^3} & -\frac{6EI}{{L_m}^2} & 0 & \frac{12EI}{{L_m}^3} & -\frac{6EI}{{L_m}^2} \\ 0 & \frac{6EI}{{L_m}^2} & \frac{2EI}{L_m} & 0 & -\frac{6EI}{{L_m}^2} & \frac{4EI}{L_m} \end{bmatrix} \tag{9}$$

$$k_e^{(g)} = T^T k_e^{(l)} T \tag{10}$$

$$T = \begin{bmatrix} R & 0 \\ 0 & R \end{bmatrix} \tag{11}$$

$$R = \begin{bmatrix} c & s & 0 \\ -s & c & 0 \\ 0 & 0 & 1 \end{bmatrix} \tag{12}$$

$$KU_e = F \tag{13}$$

$$U_e = [u_i \quad v_i \quad \theta_i \quad u_j \quad v_j \quad \theta_j]^T \tag{14}$$

$$u_e^l = T\, U_e \tag{15}$$

$$f_e^l = k_e^l\, u_e^l \tag{16}$$

$$f_e^l = [N_i \quad V_i \quad M_i \quad N_j \quad V_j \quad M_j]^T \tag{17}$$

For member force recovery, the element displacement vector in global coordinates U_e was assembled from the nodal displacement components at the element end nodes i and j. At node i, u_i and v_i were the horizontal and vertical translations and θ_i is the nodal rotation. At node j, u_j and v_j were the horizontal and vertical translations and θ_j is the nodal rotation. The corresponding local displacement vector u_e^l was obtained by transforming U_e into the element local coordinate system. The element end force vector in local coordinates was denoted by f_e^l. Its components N_i and N_j were the axial end forces, V_i and V_j are the shear end forces, and M_i and M_j are the bending end moments at the two element ends.

2.3.3. Applied Loads

Wind actions obtained from CFD were applied to the truss as equivalent distributed line loads along the top chord members of the left and right roof halves, as shown in Figure 6. Nodal displacements were obtained by solving the global equilibrium Equations. Member internal forces were then recovered from the element responses. From these results, the member axial force N, shear force V, and bending moment M were extracted and reported for all members.

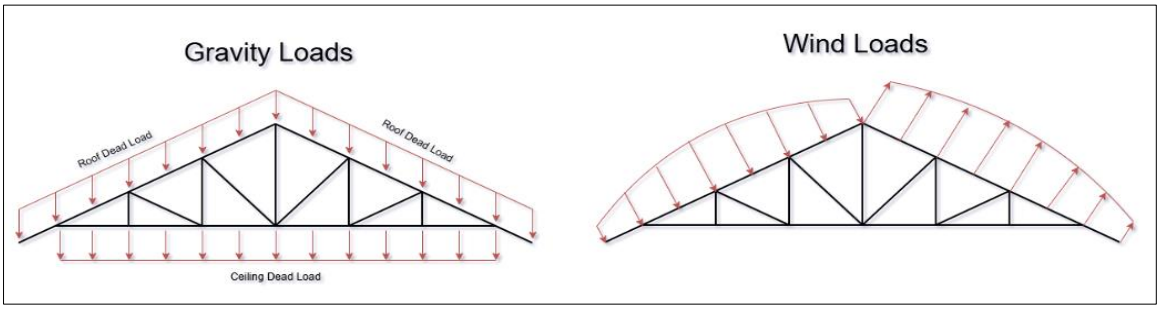

Figure 6. Application of loads

Figure 6 illustrates the loading idealization used in the MATLAB frame model. The roof truss was subjected to wind actions obtained from CFD and gravity actions from roof and ceiling dead loads. The CFD results provided the varying load to be applied on the roof. These total forces were converted into equivalent line loads along the corresponding top chord length so that the same resultant force was applied to the structural model. Roof dead load was applied as a uniform vertical downward line load along the full top chord including the overhang segments. Ceiling dead load was applied as a uniform vertical downward line load along the bottom chord between supports. The support conditions were modeled by restraining horizontal and vertical translations, while allowing rotation at both supports. This loading and support idealization produced the nodal load vector used in the global equilibrium solution.

In Figure 6, the gravity loads were modeled as uniform distributed line loads. Roof dead load was applied uniformly along the top chord and ceiling dead load was applied uniformly along the bottom chord. The dead load intensity used in the structural model was 0.48 kN per meter based on NSCP 2015 [29] and was kept constant for all design candidates. In contrast, wind loading was geometry dependent because the CFD solution changed with roof shape. In this study, the spatially varying roof pressure field from CFD is applied to the roof truss.

2.4. Particle Swarm Optimization (PSO) Implementation in MATLAB

The roof truss geometry was optimized using a custom particle swarm optimization (PSO) algorithm implemented in MATLAB. The optimization was coupled directly to the geometry generation and wind load simulation workflow so that each candidate design produced an updated SpaceClaim model, a new CFD run in ANSYS Fluent through Workbench, and a corresponding structural analysis in MATLAB. This direct coupling ensured that the selected geometry is optimal with respect to the computed wind force resultants and the structural response model used in this study. Figure 1 presents the closed loop evaluation procedure used in each particle assessment, from design variable decoding to logging of the computed objective value.

2.4.1. Objective Function and Fitness Function

The optimization objective was to minimize the maximum member utilization produced by the structural analysis. The fitness function is defined in Equation 18, where the function value is the peak utilization among all truss members for the applied wind and dead loads computed for the current geometry.

$$\text{Minimize } f(\text{x}) = \text{maxUtil(x)} \tag{18}$$

The present study used a single-objective formulation because the main purpose was to develop and demonstrate the coupled CFD-PSO workflow for reducing the critical member demand in a bamboo roof truss. The maximum member utilization was selected as the objective function because it directly represents the highest demand-to-capacity ratio among the truss members under the combined CFD-derived wind loads and gravity loads. Although deflection and truss volume were monitored during the optimization, they were not included as separate objective functions in the present formulation. A multi-objective formulation involving utilization, deflection, material volume, cost, constructability, and reliability would provide a more comprehensive design assessment, but this was outside the scope of the present study. Future work should extend the framework to multi-objective optimization to evaluate trade-offs among safety, serviceability, and material efficiency.

2.4.2. Design Variables

Each candidate solution was represented using three design variables. These include the ridge height h_r and two dimensionless ratios r_1 and r_2 that that govern the horizontal placement of the internal vertical members on one half span. The ridge height h_r directly controls the roof slope and truss depth, which in turn affects both the aerodynamic forcing and the structural stiffness and force distribution. The ratios r_1 and r_2 are used to define the panel segment lengths on the left half span. Specifically, r_1 scales the first segment length L_1 as defined in Equation 1, and r_2 scales the second segment length L_2 as defined in Equation 2. These segment lengths locate the interior panel points along the bottom chord, which then define the corresponding vertical member locations used in the truss generation, while the right half of the truss is obtained by mirroring about midspan. Table 2 summarizes the design variables and the bounds used in the search.

Table 2. Design variables and bounds used in the optimization.

Variable	Description	Lower bound	Upper bound
h_r	Ridge rise above eave level in meters	0.60	2.50
r_1	Ratio for first interior vertical on left half span	0.05	0.95
r_2	Ratio for second interior vertical on left half span	0.05	0.95

2.4.3. Feasibility Constraints

A feasibility screening step was used before running SpaceClaim and Workbench to avoid spending time on geometries that are not practical or that can cause unstable structural analysis. The screening was applied after the ratio variables r_1 and r_2 were decoded into the half span segment lengths L_1, L_2, and L_3 as shown in Figure 3 and defined in Equations 1 to 3. The corresponding vertical member locations on the left half span were then established using these segment lengths.

Simple geometric rules were enforced. The first interior vertical member was kept away from the support region, and the second interior vertical member was kept away from the midspan region using an end clearance. A minimum spacing requirement was also enforced so that the two interior vertical members do not become too close. These rules prevent very short members and reduce the likelihood of numerical instability in the stiffness matrix. The feasibility conditions are given in Equations 19 to 22, where x_A is the support coordinate, x_K is the midspan coordinate, x_{V1} and x_{V2} are the decoded vertical member locations, c_e is the end clearance, and c_g is the minimum spacing.

$$x_{V1} \geq x_A + c_e \quad (19)$$

$$x_{V2} \leq x_K - c_e \quad (20)$$

$$x_{V2} > x_{V1} \quad (21)$$

$$x_{V2} - x_{V1} \geq c_g \quad (22)$$

In this study, $c_e = 0.30$ m and $c_g = 0.30$ m. If any condition was violated, the evaluation was stopped and a large penalty value was assigned to the fitness, so the swarm moves away from infeasible designs.

2.4.4. PSO Parameters

The PSO parameters were selected to produce stable convergence while keeping the total number of CFD coupled evaluations within a practical range. In this study, each particle evaluation requires geometry regeneration, a CFD run, and a structural analysis, so the number of evaluations grows directly with the swarm size and the number of iterations. For this reason, the parameter settings were chosen as a balance between search diversity and computational cost.

The swarm size was set to 30 particles. This provides enough variety of candidate geometries in each iteration to explore the three variable design space, while keeping the number of CFD evaluations manageable. The maximum number of iterations was set to 150 as an upper limit. In practice, the run is expected to stop earlier using the stall-based stopping criterion described in the next subsection, so the maximum iteration count serves mainly as a safety cap. The inertia weight and the acceleration coefficients control how particles move. The inertia weight controls how much of the previous velocity is carried into the next step, while the cognitive coefficient controls how strongly a particle is pulled toward its own best solution, and the social coefficient controls how strongly it is pulled toward the best solution found by the entire swarm. At each iteration, the velocity and position of each particle were updated using the standard PSO update Equations given in Equations 23 and 24. Equation 23 computes the new velocity based on the inertia term and the cognitive and social attraction terms. Equation 24 then updates the particle position by adding the updated velocity to the current position. Random numbers between zero and one were included in the cognitive and social terms to maintain diversity in particle movement. After each update, the design variables were clamped to their lower and upper bounds to keep all candidates within the defined search space. A fixed random seed was used to make the initial swarm generation reproducible, which supports verification and consistent comparison of repeated runs.

$$\mathrm{V}_i^{t+1} = w\mathrm{V}_i^t + c_1\mathrm{r}_1 \odot (\mathrm{pBest}_i - \mathrm{X}_i^t) + c_2\mathrm{r}_2 \odot (\mathrm{gBest} - \mathrm{X}_i^t) \quad (23)$$

$$\mathrm{X}_i^{t+1} = \mathrm{X}_i^t + \mathrm{V}_i^{t+1} \quad (24)$$

where, X_i^t is the position vector of particle $i$at iteration $t$and contains the three design variables h_r, r_1, and r_2. V_i^t is the velocity vector of particle $i$at iteration t. $w$is the inertia weight. $c_1$is the cognitive coefficient and $c_2$is the social coefficient. $pBest_i$is the best position previously found by particle i, and $gBest$ is the best position found by the entire swarm. u_1 and u_2 are vectors of random numbers uniformly distributed between zero and one and are regenerated at each update. The symbol $\odot$ denotes element wise multiplication. Equation 22 updates the particle position by adding the updated velocity to the current position.

2.4.5. Stopping Criterion

The optimization was terminated using a stall-based stopping rule to avoid unnecessary CFD evaluations once improvements become negligible. Specifically, the run stopped when the improvement in the global-best objective value between successive iterations falls below a prescribed tolerance for a specified number of consecutive iterations as dictated by Equation 25.

$$F_{best}{}^{k} - F_{best}{}^{k-1} < 10^{-3} \quad (25)$$

where F_{best}^{k} was the best (minimum) objective value found up to iteration k, 10^{-3} is the stall tolerance. S is the stall limit defined as the number of consecutive iterations for which the improvement must remain below tolerance before the optimization is terminated. In this study, the stall limit was set to S = 10.

3. Results and Discussion

The optimization objective was to minimize the maximum member utilization produced by the MATLAB structural analysis under combined CFD derived wind loads and dead loads. The PSO run completed 22 iterations with 30 particles per iteration, resulting in a total of 660 objective evaluations. The run terminated using the stall-based stopping criterion because the global best value no longer improved beyond the tolerance for the required number of consecutive iterations. The final global best improved by 37 percent relative to the best solution obtained in the first iteration.

3.1. CFD Flow and Pressure Fields of the Optimized Roof Geometry

Colored contour plots were extracted from the CFD model to further examine the wind-flow behavior around the optimized roof geometry. The contours were obtained for the best performing design with h_r = 2.079 m, r_1 = 0.324, and r_2 = 0.487. Figure 7 shows the static pressure contour, while Figure 8 shows the velocity magnitude contour around the optimized roof profile.

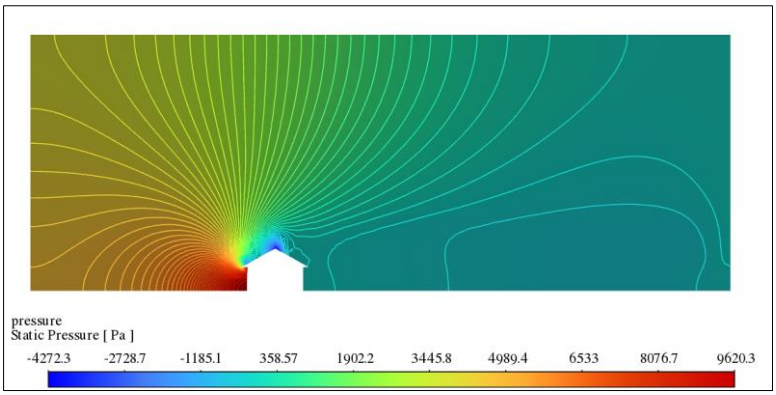

Figure 7. Static pressure contour around the optimized roof geometry

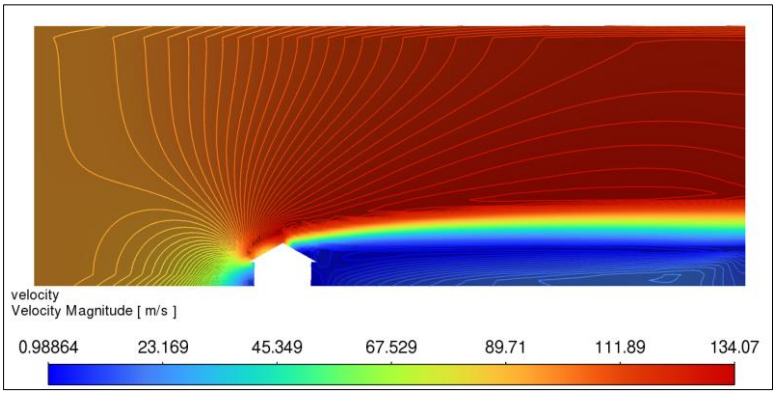

Figure 8. Velocity magnitude contour around the optimized roof geometry

As shown in Figure 7, the pressure field is not uniform along the roof surface. A high-pressure region develops near the windward side and lower region of the house envelope, while suction occurs near the roof surface and around the leeward roof region. This pressure variation explains why the wind force resultants acting on the roof changed with the roof geometry during the optimization process. The result supports the use of geometry-dependent CFD force resultants instead of applying a fixed wind pressure pattern to all candidate roof shapes.

Figure 8 shows that the wind velocity increases around the roof profile, particularly along the upper flow region and near the roof surface where the incoming wind is redirected by the pitched roof. The velocity distribution also shows the development of a lower-velocity region downstream of the roof, indicating the influence of the roof geometry on the surrounding flow field. These CFD contours provide a visual explanation for the pressure and suction behavior observed in the wind force resultants. Therefore, the contour results support the coupled CFD-PSO workflow adopted in this study, where aerodynamic demand and structural response are updated for each candidate geometry.

3.2. PSO Convergence Behavior

The PSO convergence behavior was evaluated by tracking the fitness evolution across iterations. Figure 9 presented the convergence history of the particle swarm optimization in terms of fitness, where fitness was defined as maximum member utilization and was therefore minimized. The red markers represented the global best fitness tracked across the run. The vertical spread represented the range of feasible solutions within each iteration and indicated whether the swarm was still exploring diverse solutions or had concentrated into a narrower region of the design space.

The plot indicated that the global best decreased rapidly during the early iterations, showing that PSO quickly identified improved configurations relative to the initial population. After this initial improvement, the global best approached a plateau. This plateau activated the stall-based stopping criterion once improvements fell below the tolerance for the required number of consecutive iterations. Overall, the convergence pattern suggested that the search reached a stable region of the design space under the bounds and feasibility rules adopted in this study.

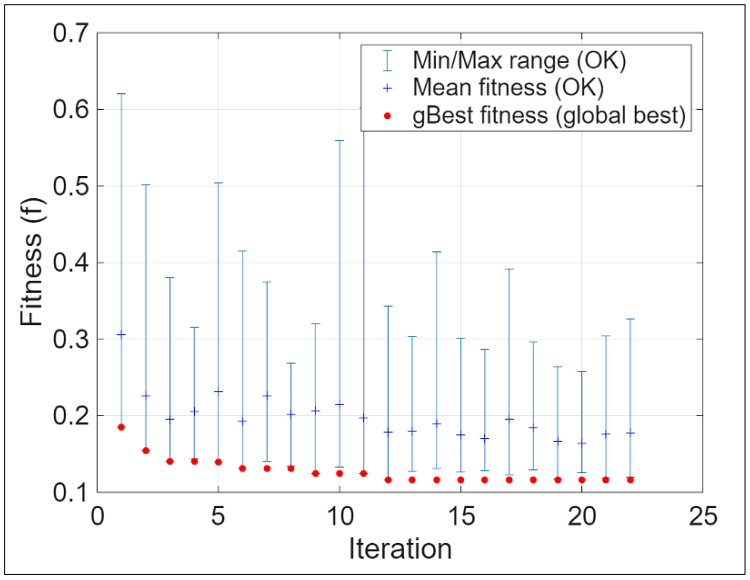

Figure 9. Minimum, maximum, and mean fitness scores in each generation

The rapid reduction in the early iterations indicates that the initial swarm contained several geometries with inefficient load paths, and that PSO was able to quickly move toward configurations with lower peak demand-to-capacity ratios. The later plateau does not necessarily indicate premature convergence but rather suggests that further changes in the design variables produced only marginal improvement within the imposed bounds and feasibility constraints. This behavior is expected in a CFD-coupled optimization problem because the aerodynamic response and structural response both change with geometry, limiting the number of highly efficient feasible regions in the design space.

3.3. Influence of Design Variable on Structural Performance

The influence of the design variables on structural performance was examined by relating the sampled values of the three variables to the resulting fitness. Figure 10 summarizes the relationship between the three design variables and the objective. The ridge height h_r controlled the roof apex elevation and truss depth, while r_1 and r_2 were dimensionless ratios that determined the horizontal placement of the two interior vertical members on the left half span through Equations 1 and 2, respectively. Since the objective was to minimize the maximum member utilization, lower values indicated a more efficient force distribution and lower demand-to-capacity ratios across members.

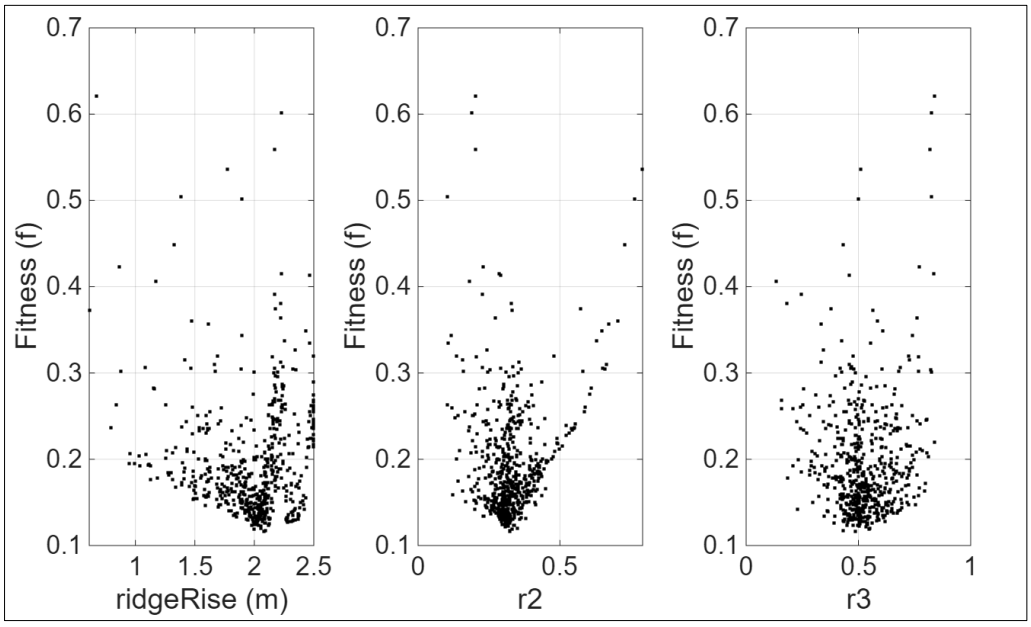

Figure 10. Design variables vs. objective

To highlight how the optimized region differs from poor performing regions, Table 3 compared the best and worst feasible solutions encountered during the run. In this implementation, fitness equals maximum member utilization, so only one of these should be reported in the table. The best design corresponds to h_r equal to 2.079 m, r_1 equal to 0.324, and r_2 equal to 0.487. This design achieved maximum member utilization equal to 0.116 with a small ridge deflection and a truss volume of approximately 0.05 m cubed. In comparison, the worst feasible design had h_r equal to 0.674 m and r_2 equal to 0.840, which resulted in maximum member utilization equal to 0.621 and a larger ridge deflection, even though the volume was slightly lower. These results indicated that improved structural performance was achieved primarily through geometry and load path changes rather than through a major increase in material volume.

Table 3. Comparison between the best and worst design.

	h_r (m)	r_1	r_2	Fitness	MaxUtil	Deflection (mm)	Volume (m^3)
Best	2.079	0.324	0.487	0.116	0.116	0.00085	0.05
Worst	0.674	0.203	0.840	0.621	0.621	0.004	0.04

The comparison between the best and worst feasible designs indicates that ridge height had a strong influence on the structural response. A higher ridge increased the truss depth, which generally improved the efficiency of axial force transfer and reduced bending demand in the members. The selected web-member location ratios also contributed to a more favorable internal load path by positioning the vertical and diagonal members in locations where the applied roof loads could be transferred more efficiently to the supports. Therefore, the reduction in maximum utilization was not caused simply by using more material, but by improving the geometric arrangement of the truss.

3.4. Evolution of Design Variables Across Iterations

Figure 11 shows how h_r evolved across iterations for the mean of feasible particles and the global best solution. h_r varies widely during the early iterations, indicating broad exploration of roof geometry. As the run progressed, the global best h_r converged and stabilized near 2.08 m, suggesting that a higher roof profile tends to produce more favorable structural performance within the explored design space. The mean h_r remained more scattered because the swarm continues to explore alternative candidates even after a stable global best region is found.

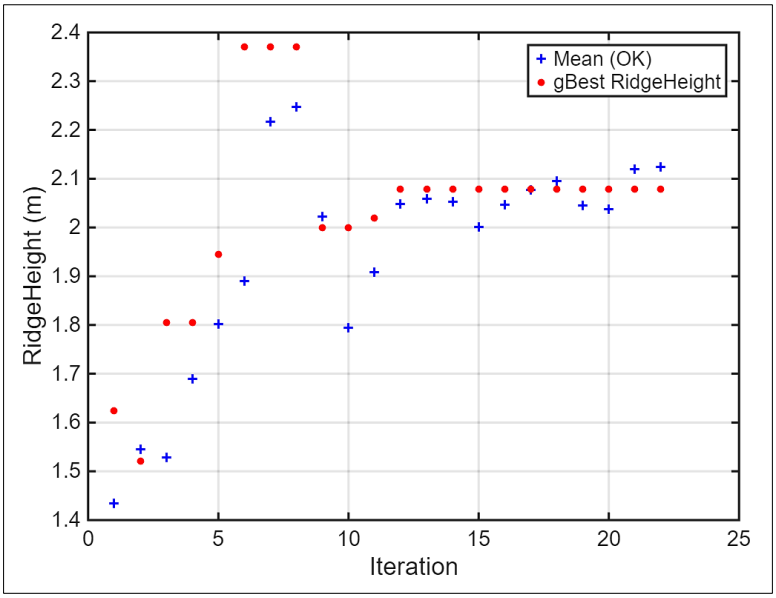

Figure 11. Influence of design variables: ridge height

Figure 12 showed the evolution of r_1 and r_2 across iterations. Both ratio variables exhibit higher variability in early iterations, reflecting exploration. Over time, the global best trajectories converged and become nearly constant around r_1 near 0.32 and r_2 near 0.49. This indicated that the best performing designs repeatedly select similar vertical member placement ratios, which suggests the presence of an effective internal web layout region for minimizing utilization.

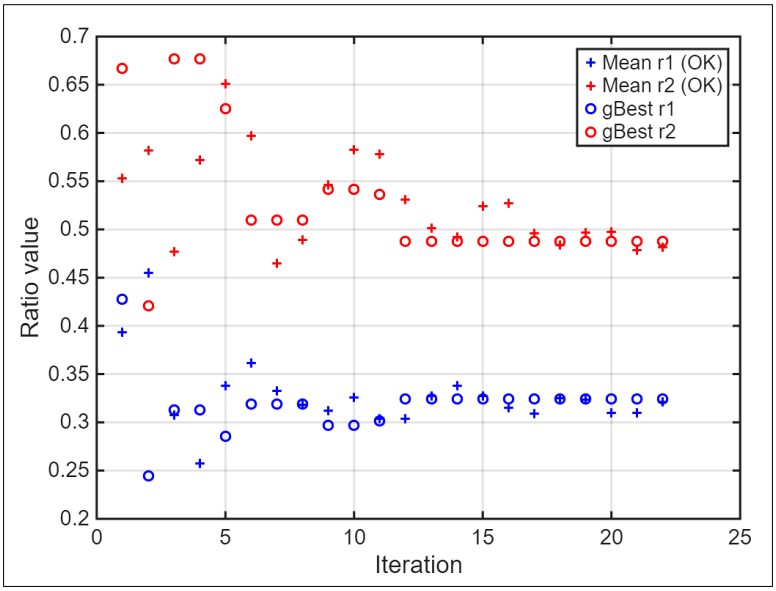

Figure 12. Influence of design variables: r_1 and r_2

3.5. Structural Response Metrics During Optimization

Figure 13 illustrated convergence using maximum member utilization for both the mean feasible solutions and the global best solution. The global best utilization dropped rapidly during the first several iterations, which indicated that PSO quickly identified substantially improved configurations. After this early improvement, the curve became nearly flat, reflecting stall behavior where further improvements are marginal. The mean utilization remains above the global best throughout the run, indicating that many particles remain non optimal while the best solution is retained.

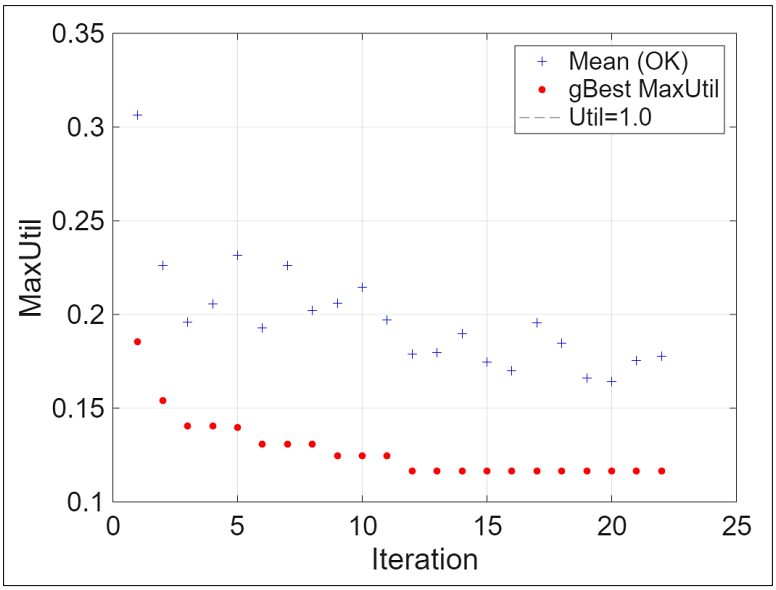

Figure 13. Global best maxUtil vs. number of Iteration (with mean maxUtil vs. Iteration)

Figure 14 showed the evolution of truss volume for the mean feasible solutions and the global best solution. Compared with maximum member utilization, the volume exhibits only small variations and stabilizes near 0.05 cubic meter in later iterations. This indicated that the improvement in utilization was not primarily driven by large increases in volume, but by finding a more favourable geometry and load path for the given truss configuration.

The nearly constant truss volume during the later iterations further supports the interpretation that the optimization improved structural efficiency mainly through shape and layout refinement. If the reduction in utilization had been caused primarily by material increase, the optimized solution would be expected to show a noticeable increase in volume. Instead, the results show that the optimized design achieved lower member utilization while maintaining a similar material quantity, which is desirable for bamboo construction where material efficiency and constructability are important.

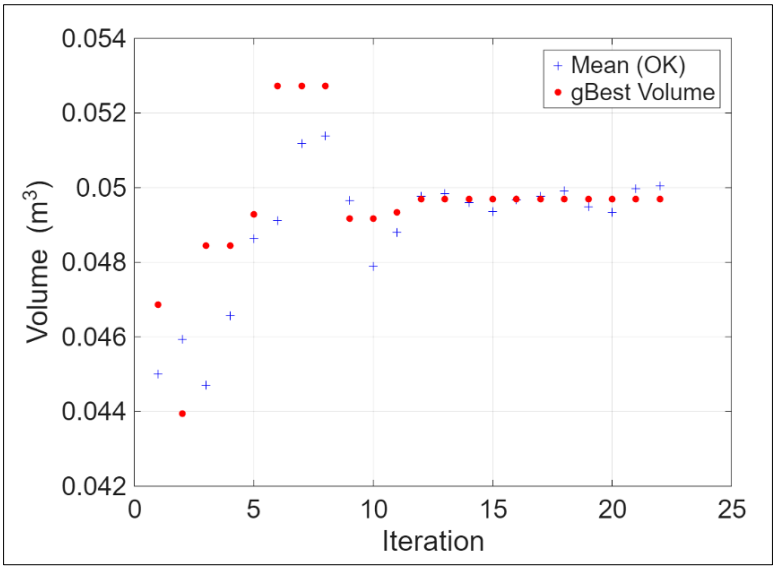

Figure 14. Global best Volume vs. number of Iteration (with mean maxUtil vs. Iteration)

3.6. Wind Force Resultants and Relationship to ridge Height

Figure 15 showed the signed resultant wind load for the global best design on the left and right roof surfaces, where positive values indicated pressure and negative values indicate suction. The wind response behavior supports the motivation for including CFD inside the optimization loop.

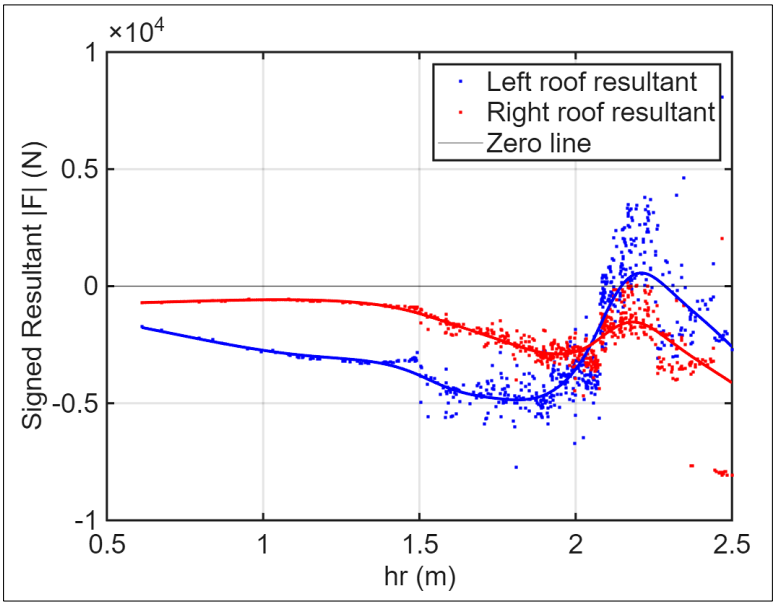

Figure 15. Roof Force Resultant vs h_r

Figure 15 relates the roof force resultants to h_r and shows a nonlinear dependence despite the scatter. At lower h_r, both the left and right roof resultants were relatively flat and remained on the suction side, indicating that changes in geometry produced only minor changes in the net wind effect. As h_r increased into the higher range, the left-roof trend rose sharply and crossed the zero line, indicating a transition from suction-dominated to pressure-dominated behavior.

In contrast, the right-roof trend remained negative, but the trend also moves to the same direction with left-roof, showing that suction persisted on the right roof even as the roof became steeper. This divergence suggests a sensitive geometry range where small increases in roof slope can reverse the direction of the resultant on one roof half while the other half does not undergo the same sign change. The clustering of points around specific h_r values further indicates that the optimization search concentrated in feasible and promising regions of the design space. Overall, the results indicate that wind demand changed with roof geometry.

The nonlinear variation of the wind force resultants demonstrates the importance of coupling CFD with the optimization loop. A fixed wind-load pattern would not capture the change in pressure and suction behavior caused by

variations in roof geometry. The observed transition between suction-dominated and pressure-dominated behavior on one roof surface indicates that small changes in ridge height can significantly affect the aerodynamic demand. This confirms that the optimized geometry was influenced not only by structural stiffness, but also by the roof-shape-dependent wind response.

3.7. Best Truss Configuration

Figure 16 shows the best-performing bamboo Howe truss from the PSO optimization, with h_r = 2.079 m, r_1 = 0.324, and r_2 = 0.487. The ratio variables define the interior vertical-member locations on the left half-span through Equations 1 to 3 and are mirrored about midspan. This geometry produced the lowest peak member utilization among feasible candidates, indicating a more efficient load path under the combined gravity and CFD-derived wind actions, without requiring a major increase in material volume.

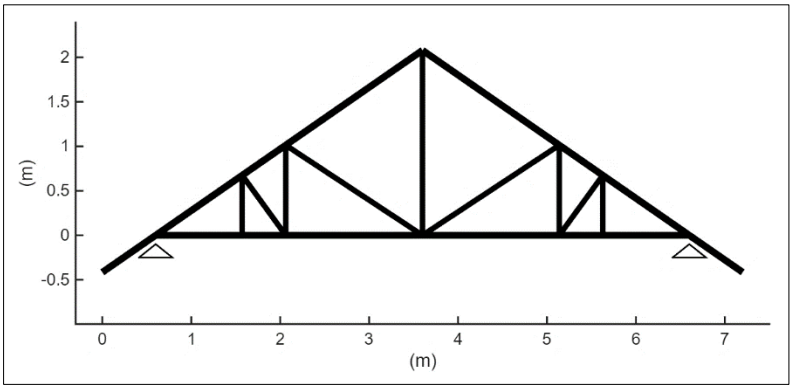

Figure 16. Best Truss Configuration

The optimized configuration represents a balance between aerodynamic demand and structural efficiency. The selected ridge height produced a roof slope that modified the wind force resultants while also increasing the structural depth of the truss. At the same time, the selected web-member ratios produced an internal layout that reduced the peak utilization among the members. This combined effect explains why the optimized design achieved lower maximum utilization without a substantial increase in truss volume.

3.8. Comparison with Previous Studies

The present study contributes mainly as a coupled computational framework for bamboo roof-truss optimization under wind loading. Previous truss optimization studies have shown that stochastic and metaheuristic algorithms can improve structural performance by changing member sizes, geometry, or layout [50–52]. However, most of these studies used prescribed external loads during the optimization process. As a result, the applied load generally remained constant even when the structural geometry changed.

CFD-based roof studies, on the other hand, have shown that roof geometry affects wind pressure, suction, and flow behavior [17, 20, 21, 39]. However, these studies commonly focus on aerodynamic assessment or the optimization of conventional building forms, rather than on the structural optimization of bamboo roof trusses. The present study connects these two areas by using CFD to compute the wind force resultants for each candidate roof geometry and then transferring these forces to a MATLAB frame model for member-utilization-based PSO optimization.

Compared with previous bamboo structural studies, which mainly focused on material characterization, connection behavior, and structural response under fixed loading, the proposed framework introduces geometry-dependent wind-load evaluation into the optimization process. This allows the aerodynamic demand and structural response to be updated together during the search. Therefore, the 37% reduction in maximum member utilization should be interpreted not only as a numerical improvement, but also as evidence that the coupled CFD-PSO workflow can identify more efficient bamboo roof-truss configurations under wind loading.

4. Conclusion

This study developed a coupled CFD and PSO workflow to improve the wind-resistant performance of a bamboo Howe roof truss. For each candidate roof geometry, ANSYS Fluent was used to compute geometry-dependent roof force resultants, which were transferred to a MATLAB two-dimensional frame model together with roof and ceiling dead loads to compute member forces and utilization. PSO was then used to identify the truss geometry that minimizes the maximum member utilization.

The PSO run converged using the stall-based stopping criterion after 660 objective evaluations over 22 iterations with 30 particles per iteration. The global best solution improved by 37 percent relative to the best solution obtained in the first iteration. The best design corresponded to h_r equal to 2.079 m with r_1 equal to 0.324 and r_2 equal to 0.487, achieving maximum member utilization equal to 0.116 while maintaining small deflection and a truss volume of approximately 0.05 m cubed. Comparison with the worst feasible design showed that utilization and deflection can be reduced without a major increase in volume, indicating that improvements were driven mainly by truss depth and load path refinement rather than added material.

The convergence histories show that the design variables stabilized as the swarm converged, and the utilization plateau aligned with the stall-based termination. The roof force resultants exhibited a nonlinear relationship with h_r and included a transition region where geometry changes affected pressure and suction behavior, supporting the need for geometry dependent wind demand in the optimization loop. Future work can extend the framework to multiple wind directions, and more detailed modeling of bamboo variability and connection behavior. The same workflow can also be expanded to include additional design variables and multi objective formulations that balance utilization, deflection, and material volume for practical design of wind resilient bamboo roof systems.

5. Declarations

5.1. Author Contributions

Conceptualization, M.J.A. and N.A.M.; methodology, M.J.A. and N.A.M.; software, M.J.A. and N.A.M.; validation, J.O. and L.E.G.; formal analysis, M.J.A. and N.A.M.; investigation, M.J.A. and N.A.M.; resources, J.O. and L.E.G.; data curation, M.J.A. and N.A.M.; writing—original draft preparation, M.J.A. and N.A.M.; writing—review and editing, J.O. and L.E.G.; visualization, M.J.A. and N.A.M.; supervision, J.O. and L.E.G.; project administration, J.O. and L.E.G.; funding acquisition, J.O. and L.E.G. All authors have read and agreed to the published version of the manuscript.

5.2. Data Availability Statement

The data presented in this study are available in the article.

5.3. Funding and Acknowledgments

The authors would like to express their sincere gratitude to the Department of Science and Technology – Science Education Institute (DOST-SEI) and the Engineering Research and Development for Technology (ERDT) program for their financial support of this research.

5.4. Conflicts of Interest

The authors declare no conflict of interest.

6. References

[1] Emaojo, E. F. (2025). Housing Crisis: Countries at Breaking Point in 2025. DevelopmentAid, Nicosia, Cyprus. Available online: https://www.developmentaid.org/news-stream/post/203238/housing-crisis-in-2025 (accessed on April 2026).

[2] UNEP. (2024). 2023 Global Status Report for Buildings and Construction: Beyond foundations - Mainstreaming sustainable solutions to cut emissions from the buildings sector. United Nations Environment Programme, Nairobi, Kenya. doi:10.59117/20.500.11822/45095.

[3] Aniñon, M. J. C., & Garciano, L. E. O. (2024). Advances in Connection Techniques for Raw Bamboo Structures—A Review. Buildings, 14(4), 1126. doi:10.3390/buildings14041126.

[4] Kumar Boity, A., Bhandari, H., & Shukla, S. (2022). Bamboo as a sustainable building construction material. Materials Today: Proceedings, 71, 306–311. doi:10.1016/j.matpr.2022.09.218.

[5] Chainey, S., Shijagurumayum, C., & Thokchom, S. (2022). Review on the Use of Bamboo as a Construction Material. SAMRIDDHI: A Journal of Physical Sciences, Engineering and Technology, 14(1), 47–51. doi:10.18090/samriddhi.v14spli01.9.

[6] Cho, E., Um, Y., Yoo, S. K., Lee, H., Kim, H. B., Koh, S., Shin, H. C., & Lee, Y. (2011). An Expressed Sequence Tag Analysis for the Fast-Growing Shoots of Bambusa edulis Murno. Journal of Plant Biology, 54(6), 402–408. doi:10.1007/s12374-011-9179-2.

[7] Yiping, L., Yanxia, L., Buckingham, K., Henley, G., & Guomo, Z. (2010). Bamboo and Climate Change Mitigation: a comparative analysis of carbon sequestration. International Network for Bamboo and Rattan, 30, 1-47.

[8] Muhammad, N. A. G., Orejudos, J. N., & Aniñon, M. J. C. (2024). A Compendium of Research, Tools, Structural Analysis, and Design for Bamboo Structures. Buildings, 14(8), 2419. doi:10.3390/buildings14082419.

[9] Pan, C., Zhou, G., Shrestha, A. K., Chen, J., Kozak, R., Li, N., Li, J., He, Y., Sheng, C., & Wang, G. (2023). Bamboo as a Nature-Based Solution (NbS) for Climate Change Mitigation: Biomass, Products, and Carbon Credits. Climate, 11(9), 175. doi:10.3390/cli11090175.

[10] Hildayanti, A., & Wasilah. (2023). Optimizing Bamboo as an Alternative Building Material to Respond Global Architectural Challenges. IOP Conference Series: Earth and Environmental Science, 1157(1), 12011. doi:10.1088/1755-1315/1157/1/012011.

[11] Masdar, A., Suhendro, B., Siswosukarto, S., & Sulistyo, D. (2017). Influence of Bolt Tightening's Force to the Strength of Connection System of Bamboo Truss Structure with Wooden Clamp. Procedia Engineering, 171, 1370–1376. doi:10.1016/j.proeng.2017.01.445.

[12] Moran, R., & García, J. J. (2019). Bamboo joints with steel clamps capable of transmitting moment. Construction and Building Materials, 216, 249–260. doi:10.1016/j.conbuildmat.2019.05.025.

[13] Paraskeva, T. S., Grigoropoulos, G., & Dimitrakopoulos, E. G. (2017). Design and experimental verification of easily constructible bamboo footbridges for rural areas. Engineering Structures, 143, 540–548. doi:10.1016/j.engstruct.2017.04.044.

[14] Villegas, L., Morán, R., & García, J. J. (2019). Combined culm-slat Guadua bamboo trusses. Engineering Structures, 184, 495–504. doi:10.1016/j.engstruct.2019.01.114.

[15] Madhushan, S., Buddika, S., Bandara, S., Navaratnam, S., & Abeysuriya, N. (2023). Uses of Bamboo for Sustainable Construction—A Structural and Durability Perspective—A Review. Sustainability (Switzerland), 15(14), 11137. doi:10.3390/su151411137.

[16] DOST-PAGASA. (2026). Troical Cyclone Information. Department of Science and Technology Philippine Atmospheric, Geophysical and Astronomical Services Administration, Quezon City, Philippine. Available online: https://www.pagasa.dost.gov.ph/climate/tropical-cyclone-information?utm_source=chatgpt.com (accessed on April 2026).

[17] Singh, J., & Roy, A. K. (2019). Effects of roof slope and wind direction on wind pressure distribution on the roof of a square plan pyramidal low-rise building using CFD simulation. International Journal of Advanced Structural Engineering, 11(2), 231–254. doi:10.1007/s40091-019-0227-3.

[18] Blocken, B. (2014). 50 years of Computational Wind Engineering: Past, present and future. Journal of Wind Engineering and Industrial Aerodynamics, 129, 69–102. doi:10.1016/j.jweia.2014.03.008.

[19] Montazeri, H., & Blocken, B. (2013). CFD simulation of wind-induced pressure coefficients on buildings with and without balconies: Validation and sensitivity analysis. Building and Environment, 60, 137–149. doi:10.1016/j.buildenv.2012.11.012.

[20] Enteria, N. A. (2016). CFD evaluation of Philippine detached structure with different roofing designs. Infrastructures, 1(1), 3. doi:10.3390/infrastructures1010003.

[21] Mata, J. L., Orejudos, J. N., Opon, J. G., & Guirnaldo, S. A. (2023). Optimizing Building Orientation and Roof Angle of a Typhoon-Resilient Single-Family House Using Genetic Algorithm and Computational Fluid Dynamics. Buildings, 13(1), 107. doi:10.3390/buildings13010107.

[22] Zhang, X., Ye, X., & Weerasuriya, A. U. (2025). CFD-based parametric study of venturi-shaped roof optimization for wind energy harvesting by building-integrated wind turbines in an idealized high-rise building. Building and Environment, 285, 113574. doi:10.1016/j.buildenv.2025.113574.

[23] Tsiptsis, I. N., Liimatainen, L., Kotnik, T., & Niiranen, J. (2019). Structural optimization employing isogeometric tools in Particle Swarm Optimizer. Journal of Building Engineering, 24, 100761. doi:10.1016/j.jobe.2019.100761.

[24] Mei, L., & Wang, Q. (2021). Structural optimization in civil engineering: a literature review. Buildings, 11(2), 66. doi:10.3390/buildings11020066.

[25] Rajput, S. P. S., & Datta, S. (2019). A review on optimization techniques used in civil engineering material and structure design. Materials Today: Proceedings, 26, 1482–1491. doi:10.1016/j.matpr.2020.02.305.

[26] Zaheer, Q., Yonggang, T., & Qamar, F. (2022). Literature review of bridge structure's optimization and it's development over time. International Journal for Simulation and Multidisciplinary Design Optimization, 13, 5. doi:10.1051/smdo/2021039.

[27] Jankowski, R., Manguri, A., Hassan, H., & Saeed, N. (2025). Topology, Size, and Shape Optimization in Civil Engineering Structures: A Review. Computer Modeling in Engineering &Amp; Sciences, 142(2), 933–971. doi:10.32604/cmes.2025.059249.

[28] Pararuan, Z. F., Perez, T. S., Pineda, K. B., Salunga, K.D., Santos, L. M., Zuniga, J. T., Lacap, L.C. S., Duya, R. O., & Tolentino, A. S. (2025). Cost-Optimized Design of Reinforced Concrete Frames for a Proposed Five-Bay, Three-Storey Academic Building at Don Honorio Ventura State University, Apalit Campus, Using a Genetic Algorithm. International Journal of Scientific Research and Engineering Development, 8(3).

[29] NSCP 2015. (2015). The National Structural Code of the Philippines. Association of Structural Engineers of the Philippines, Quezon City, Philippines.

[30] Lee, K. J., Huang, Y., & Mueller, C. T. (2025). A differentiable structural analysis framework for high-performance design optimization. Structures, 78. doi:10.1016/j.istruc.2025.109292.

[31] Zhuang, Z., Xie, Y. M., Li, Q., & Zhou, S. (2023). A 172-line Matlab code for structural topology optimization in the body-fitted mesh. Structural and Multidisciplinary Optimization, 66(1), 11. doi:10.1007/s00158-022-03464-x.

[32] Belz, J., & Kromoser, B. (2025). Structural optimization of wooden building components: a systematic review of established practices. Wood Material Science & Engineering, 1–22. doi:10.1080/17480272.2025.2525328.

[33] Kennedy, J., & Eberhart, R. (1995). Particle swarm optimization. Proceedings of ICNN'95-international conference on neural networks, 27 November-1 December, 1995, Perth, Australia

[34] Azanaw, G. M. (2025). Design Optimization in Structural Engineering: A Systematic Review of Computational Techniques and Real-World Applications. American Journal of Mechanical and Materials Engineering 9(1), 11. doi:10.11648/j.ajmme.20250901.11.

[35] Mortazavi, A., & Toğan, V. (2017). Sizing and layout design of truss structures under dynamic and static constraints with an integrated particle swarm optimization algorithm. Applied Soft Computing Journal, 51, 239–252. doi:10.1016/j.asoc.2016.11.032.

[36] Cao, H., Qian, X., Chen, Z., & Zhu, H. (2017). Enhanced particle swarm optimization for size and shape optimization of truss structures. Engineering Optimization, 49(11), 1939–1956. doi:10.1080/0305215X.2016.1273912.

[37] Li, Y., Peng, Y., & Zhou, S. (2013). Improved PSO algorithm for shape and sizing optimization of truss structure. Journal of Civil Engineering and Management, 19(4), 542–549. doi:10.3846/13923730.2013.786754.

[38] Hosseini, S. S., Hamidi, S. A., Mansuri, M., & Ghoddosian, A. (2015). Multi objective particle swarm optimization (MOPSO) for size and shape optimization of 2D truss structures. Periodica Polytechnica Civil Engineering, 59(1), 9–14. doi:10.3311/PPci.7341.

[39] Xin, L., Zhou, X., & Gu, M. (2022). Wind tunnel test and CFD simulation of the near-roof wind speed and friction velocity on gable roofs. Journal of Wind Engineering and Industrial Aerodynamics, 225, 105009. doi:10.1016/j.jweia.2022.105009.

[40] Sudin, R., & Swamy, N. (2006). Bamboo and wood fibre cement composites for sustainable infrastructure regeneration. Journal of materials science, 41(21), 6917-6924. doi:10.1007/s10853-006-0224-3.

[41] Adier, M. F. V., Sevilla, M. E. P., Valerio, D. N. R., & Ongpeng, J. M. C. (2023). Bamboo as Sustainable Building Materials: A Systematic Review of Properties, Treatment Methods, and Standards. Buildings, 13(10), 2449. doi:10.3390/buildings13102449.

[42] Nguyen, T. T., Pham, H. T., & Nguyen, H. K. (2025). Data-Driven Approach to Predict Fire-Resistance Ratings of Timber Columns. Civil Engineering Journal, 11(10), 4232–4245. doi:10.28991/CEJ-2025-011-10-013.

[43] Cacanando, C. J. D., López, L. F., Atienza, E., & Pradhan, N. P. N. (2025). Experimental characterization of mechanical properties of Bambusa blumeana bamboo poles and determination of design values. Construction and Building Materials, 490, 142498. doi:10.1016/j.conbuildmat.2025.142498.

[44] Bangoy, C. D. O., Falcon, J. Y., Lorenzo, H. A. F., Zeng, S. R. A., Garciano, L. E. O., & Cacanando, C. J. D. (2024). Experimental Study on the Dowel-Bearing Strength of Bambusa blumeana Bamboo Used for Sustainable Housing Construction. Sustainability (Switzerland), 16(13), 5530. doi:10.3390/su16135530.

[45] Dara, S. K., Peace, H. S., Djoui, T., Doko, K. V., & Gibigaye, M. (2025). Experimental Study on the Identification and Mechanical Characterization of Local Bamboo from Benin for Its Use in Wood-Concrete Composite Structures. World Journal of Engineering and Technology, 13(04), 923–933. doi:10.4236/wjet.2025.134057.

[46] Ruijia, W. U., Ke, M. A., Pengyu, L. I., Yubing, H. O. U., Peixiang, W. A. N. G., Binbin, L. I., & Yan, X. I. A. O. (2024). Experimental and numerical studies on a glubam spherical dome. Engineering Structures, 303, 117462. doi:10.1016/j.engstruct.2024.117462.

[47] Sulistiana, P. D., Ketut Yasa Bagiarta, I., Nengah Sinarta, I., Putra, I. B. G. P., Bili, H. T., & Dewi, D. A. R. S. (2025). Structural Performance Evaluation of Bamboo Shelters as Temporary Housing Solutions. IOP Conference Series: Earth and Environmental Science, 1488(1), 12026. doi:10.1088/1755-1315/1488/1/012026.

[48] Zhang, X., Sheng, Y., Zhao, E., Yin, H., Li, S., Li, S., & Liu, Q. (2024). Experiment and finite element analysis on load-carrying performance of double-shear connections of inorganic-bonded bamboo composite. Journal of Building Engineering, 85, 108756. doi:10.1016/j.jobe.2024.108756.

[49] Association of Structural Engineers of the Philippines. (2025). Philippine Guidelines on Bamboo Design and Construction. Association of Structural Engineers of the Philippines, Quezon City, Philippines.

[50] Avcı, M. S., Yavuz, D., Ercan, E., & Nuhoğlu, A. (2024). Efficient Sizing and Layout Optimization of Truss Benchmark Structures Using ISRES Algorithm. Applied Sciences (Switzerland), 14(8), 3324. doi:10.3390/app14083324.

[51] Chamoret, D., Qiu, K., & Domaszewski, M. (2009). Optimization of truss structures by a stochastic method. International Journal for Simulation and Multidisciplinary Design Optimization, 3(1), 321–325. doi:10.1051/ijsmdo:2009005.

[52] Khodadadi, N., Çiftçioğlu, A. Ö., Mirjalili, S., & Nanni, A. (2023). A comparison performance analysis of eight meta-heuristic algorithms for optimal design of truss structures with static constraints. Decision Analytics Journal, 8, 100266. doi:10.1016/j.dajour.2023.100266.